

How perturbative QCD constrains the Equation of State at Neutron-Star densities

Oleg Komoltsev¹ and Aleksi Kurkela^{1,2}

¹*Faculty of Science and Technology, University of Stavanger, 4036 Stavanger, Norway*

²*Univ Lyon, Univ Claude Bernard Lyon 1, CNRS/IN2P3, IP2I Lyon, UMR 5822, F-69622, Villeurbanne, France*

We demonstrate in a general and analytic way how high-density information about the equation of state (EoS) of strongly interacting matter obtained using perturbative Quantum Chromodynamics (pQCD) constrains the same EoS at densities reachable in physical neutron stars. Our approach is based on utilizing the full information of the thermodynamic potentials at the high-density limit together with thermodynamic stability and causality. The results can be used to propagate the pQCD calculations reliable around $40n_s$ to lower densities in the most conservative way possible. We constrain the EoS starting from only few times the nuclear saturation density $n \gtrsim 2.2n_s$ and at $n = 5n_s$ we exclude at least 65% of otherwise allowed area in the $\epsilon - p$ -plane. These purely theoretical results are independent of astrophysical neutron-star input and hence they can also be used to test theories of modified gravity and BSM physics in neutron stars.

I. INTRODUCTION

The rapid evolution of neutron-star (NS) astronomy in recent years — in particular the recent NS radius measurements [1, 2], the discovery of massive NSs [3–5], and the advent of gravitational-wave and multi-messenger astronomy [6, 7] — is for the first time giving us empirical access to the physics of the cores of NSs. Within the Standard Model and assuming general relativity, the internal structure of NSs is determined by the equation of state (EoS) of strongly interacting matter [8, 9]. With these assumptions, NS observations can be used to empirically determine the EoS [10–30] (for reviews, see [31–37]). And if the EoS can be determined theoretically to a sufficient accuracy, comparison with NS observations allows to use these extreme objects as laboratory for physics beyond standard model (see, e.g., [38–46]) and/or general relativity (e.g., [47–51]).

For both of these goals, it is crucial to make use of all possible controlled theory calculations that inform us about the EoS at densities reached in NSs. While in principle the EoS is determined by the underlying theory of strong interactions, Quantum Chromodynamics (QCD), in practice we have access to the EoS only in limiting cases. In the context of low temperatures relevant for neutron stars, the EoS of QCD can be systematically approximated at low- and at high-density limits. At low densities, the current state-of-the-art low-energy effective theory calculations allow to describe matter to densities around and slightly above nuclear saturation density $n \approx n_s = 0.16/\text{fm}^3$ [52, 53], but become unreliable at higher densities $n \sim 5 - 10n_s$ reached in the cores of massive neutron stars. A complementary description of NS matter comes from perturbative QCD (pQCD) calculations which become reliable at sufficiently high densities $\sim 40n_s$, far exceeding those realised in NSs [54, 55].

Several works have used large ensembles of parameterized EoSs to study the possible behavior of the EoS in intermediate densities between the theoretically known limits. Many of these works have anchored their EoS to

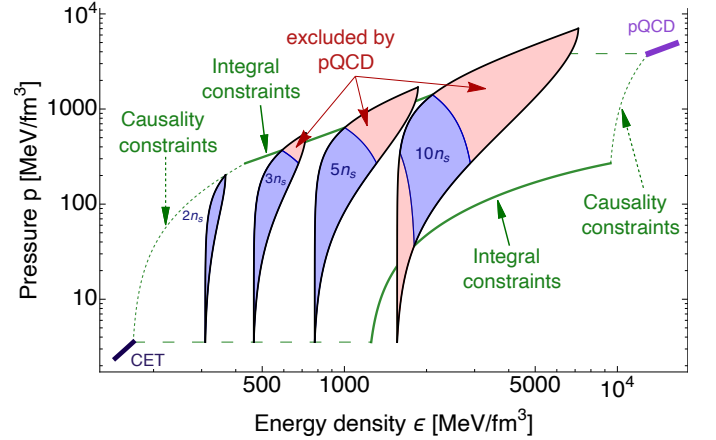


FIG. 1. Theoretical constraints to ϵ and p arising from low- (CET) and high-density input (pQCD). The green lines show the envelope of allowed values of $p(\epsilon)$; dashed green lines arise from trivially imposing causality of the EoS while the thick solid lines correspond to newly identified integral constraints arising from imposing simultaneously the high-density limit for p , n , and μ . The blue regions correspond to allowed values ϵ and p at fixed density n ; the red regions would be otherwise allowed but are excluded by the high-density input. At $n = 5n_s$, 75% of otherwise allowed values of ϵ and p are excluded by the high-density input.

the low-density limit only, while others have interpolated between the two orders of magnitude in density separating the low- and high-density limits [10, 16, 27, 56, 57]. While the input from pQCD clearly constrains the EoS at very high densities, how this information affects the EoS around neutron-star densities has so far been convoluted by the specific choices of interpolation functions.

The aim of the present work is to make the influence of the high-density calculations to the EoS at intermediate densities explicit, and in particular, to derive constraints to the EoS that are completely independent of any specific interpolation function. By using the full information available in the thermodynamic grand canoni-

cal potential as a function of baryon chemical potential, $\Omega(\mu) = -p(\mu)$, we find stricter bounds than works using only the reduced form of the EoS, i.e., the pressure as a function of energy density $p(\epsilon)$ appearing in the hydrodynamic description of neutron star matter [51, 58–61]. The effect is demonstrated in fig. 1, which shows the region in $\epsilon - p$ -plane that can be reached with a causal and thermodynamically stable EoS with information of the high-density limit, and in particular compares the allowed values at different fixed densities $n = 2, 3, 5$, and $10n_s$ with and without the pQCD input.

II. SETUP

In the following we consider all possible interpolations of the full thermodynamic potential at zero temperature and in β -equilibrium, $\Omega(\mu) = -p(\mu)$, between the low-density limit $\mu = \mu_L$ and the high-density limit $\mu = \mu_H$. We assume that at both of these limits the pressure $p(\mu)$ and its first derivative, baryon number density $n(\mu) = \partial_\mu p(\mu)$ are known

$$p(\mu_L) = p_L, \quad p(\mu_H) = p_H, \quad (1)$$

$$n(\mu_L) = n_L, \quad n(\mu_H) = n_H. \quad (2)$$

This information is readily available from the microscopic calculations which are assumed to be reliable at these limits; representative values from state-of-the-art chiral effective theory (CET) [62] and pQCD calculations [55] from the literature are reproduced in table I.

Thermodynamic consistency requires that pressure is a continuous function of μ . Similarly, thermodynamic stability requires convexity of thermodynamic potentials $\partial_\mu^2 \Omega \leq 0$ so that $n(\mu)$ is a monotonically increasing function $\partial_\mu n(\mu) \geq 0$. Density $n(\mu)$ does not need to be continuous and it can have discontinuities (increasing the density at fixed μ) in the case of 1st-order phase transitions; we place no additional assumptions on the number or strength of possible transitions. Causality requires that the speed of sound is less than the speed of light, $c_s^2 \leq 1$, and it imposes a condition on the first derivative of the number density

$$c_s^{-2} = \frac{\mu}{n} \frac{\partial n}{\partial \mu} \geq 1. \quad (3)$$

We construct the allowed EoSs by considering all possible functions $n(\mu)$ allowed by the above assumptions connecting the low- and high-density limits. Causality imposes a minimal allowed slope of the number density, i.e., $\partial_\mu n(\mu) \geq n/\mu$, that any causal EoS passing through a given point in the $\mu - n$ plane can have. This can be visualized as a vector field on the $\mu - n$ plane as depicted in fig. 2, where the arrows at each point corresponds to tangent lines with constant $c_s^2 = 1$. This requirement imposes two fundamental constraints on the $\mu - n$ plane. Starting from the point $\{\mu_L, n_L\}$ we can follow the arrows until μ_H by solving eq. (3) with $c_s^2 = 1$, leading to

	CET		pQCD		
	soft	stiff	$X = 1$	$X = 2$	$X = 4$
μ [GeV]	0.966	0.978	2.6		
n [1/fm ³]	0.176		6.14	6.47	6.87
p [MeV/fm ³]	2.163	3.542	2334.	3823.	4284.

TABLE I. Collection of predictions for the thermodynamic quantities at the low- (CET) and the high- (pQCD) density limits. CET limit corresponds to the "stiff" and "soft" EoS of [62] while the pQCD values are from a partial N3LO calculation [55] at three different values of the renormalization scale parameter X . The uncertainty of the pQCD limit can be assessed by varying X in the range $X = [1, 4]$. All figures correspond to the "stiff" CET and $X = 2$ pQCD.

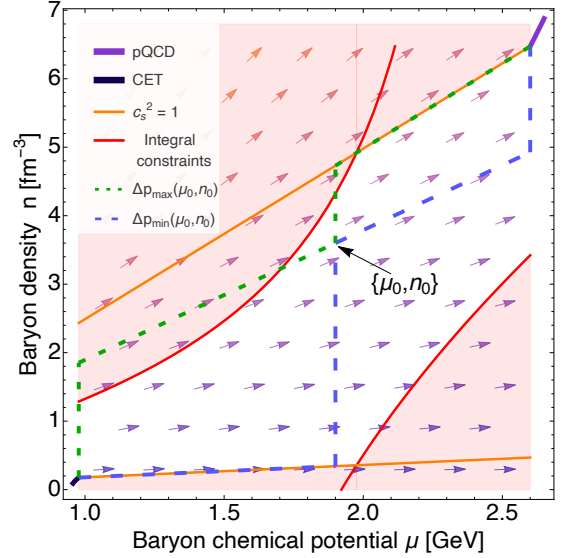


FIG. 2. Density as a function of chemical potential determines the EoS. At any given point $\{\mu, n\}$, causality imposes a minimal slope to any EoS passing that point $\partial_\mu n(\mu) \geq \frac{n}{\mu}$, denoted by the arrows. Thermodynamic consistency demands that $n(\mu)$ is a monotonic function, and that the area under the curve in the plot is given by Δp . These conditions cannot be simultaneously fulfilled by any EoS that passes to the red area at any density and are therefore excluded. The lines Δp_{\min} and Δp_{\max} display the constructions defined in eq. (5) and eq. (8).

$n(\mu) = n_L \mu / \mu_L$. This produces a maximally stiff causal EoS and the area under this line cannot be reached from the low-density limit with a causal EoS. Correspondingly, upper limit for the $n(\mu)$ can be obtained starting from $\{\mu_H, n_H\}$ and following the arrows backward to μ_L ; the high-density limit n_H cannot be reached from any point above this line by a causal EoS. These previously known bounds (e.g. [51, 58]) are represented as orange lines in fig. 2.

The simultaneous requirement of reaching both p_H and n_H imposes further constraints and fixes the area under

the curve $n(\mu)$.

$$\int_{\mu_L}^{\mu_H} n(\mu) d\mu = p_H - p_L = \Delta p. \quad (4)$$

In the example shown in fig. 2, this requirement imposes that the area under any allowed EoS is approximately one third of the area of the figure.

At each point we can evaluate the absolute minimum and maximum area under any EoS ($\Delta p_{\min/\max}$) that can be reached at μ_H if the EoS goes through that particular point. If Δp_{\min} (Δp_{\max}) is bigger (smaller) than Δp then such point would be ruled out.

To obtain the minimum area at μ_H for any EoS going through a specific point $\{\mu_0, n_0\}$ consider the following construction shown in fig. 2 as a dashed blue line

$$n(\mu) = \begin{cases} n_L \mu / \mu_L, & \mu_L < \mu < \mu_0 \\ n_0 \mu / \mu_0, & \mu_0 < \mu < \mu_H. \end{cases} \quad (5)$$

For $\mu < \mu_0$, the smallest possible area is determined by the maximally stiff causal line (i.e. $c_s^2 = 1$) starting from $\{\mu_L, n_L\}$ which we follow up to μ_0 . At μ_0 , we have a phase transition where the density jumps to n_0 . After that, the EoS follows the maximally stiff causal line starting at $\{n_0, \mu_0\}$ until μ_H , where the EoS has another phase transition to reach $n(\mu_H) = n_H$. The solution to the equation $\Delta p_{\min}(\mu_0, n_0) = \int_{\mu_L}^{\mu_H} n(\mu) d\mu = \Delta p$ is shown in fig. 2 as the top red line denoted integral constraints; any EoS crossing this line is inconsistent with simultaneous constraint on p_H and n_H . This yields a maximum density for given μ

$$n_{\max}(\mu) = \begin{cases} \frac{\mu^3 n_L - \mu \mu_L (\mu_L n_L + 2\Delta p)}{(\mu^2 - \mu_H^2) \mu_L}, & \mu_L \leq \mu < \mu_c \\ n_H \mu / \mu_H, & \mu_c \leq \mu \leq \mu_H, \end{cases} \quad (6)$$

where μ_c is given by the intercept of the causal line and the integral constraint, i.e., the two cases in eq. (6)

$$\mu_c = \sqrt{\frac{\mu_L \mu_H (\mu_H n_H - \mu_L n_L - 2\Delta p)}{\mu_L n_H - \mu_H n_L}}. \quad (7)$$

Similarly, the procedure to maximize area under any EoS going through the point $\{n_0, \mu_0\}$ is shown as a dashed green line in fig. 2,

$$n(\mu) = \begin{cases} n_0 \mu / \mu_0, & \mu_L < \mu < \mu_0 \\ n_H \mu / \mu_H, & \mu_0 < \mu < \mu_H. \end{cases} \quad (8)$$

Correspondingly, solving for $\Delta p_{\max} = \Delta p$ gives a constraint to the minimal n that can be obtained for a given μ , depicted as the bottom red line in fig. 2. Then, for a given chemical potential the minimal allowed density is

$$n_{\min}(\mu) = \begin{cases} n_L \mu / \mu_L, & \mu_L \leq \mu \leq \mu_c \\ \frac{\mu^3 n_H - \mu \mu_H (\mu_H n_H - 2\Delta p)}{(\mu^2 - \mu_L^2) \mu_H}, & \mu_c < \mu \leq \mu_H. \end{cases} \quad (9)$$

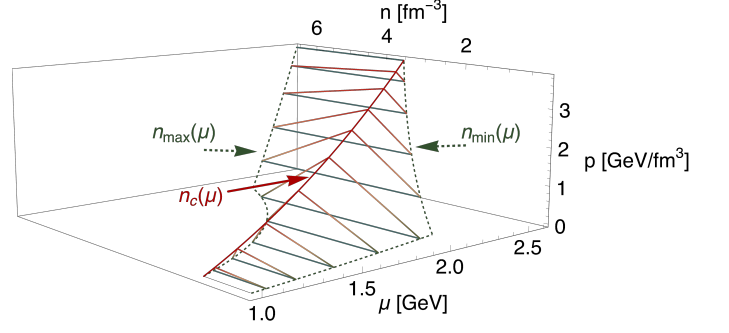


FIG. 3. 3D rendering of the constraints in the $\mu - n - p$ phase space. Each triangle is a slice of the $p - n$ constraints for fixed μ . Note that n_{\max} , n_{\min} and n_c , which are defined in eq. (6), eq. (9), and eq. (11), respectively, are projection on the $\mu - n$ -plane of the lines denoted with the same names in the figure above.

Note that the maximally stiff causal lines intercept with the integral constraints at the same point μ_c for lower and upper limits. This happens because the EoS following $n_{\min}(\mu)$ up to μ_c obtains the correct area Δp only if the EoS jumps at μ_c from $n_{\min}(\mu_c)$ to $n_{\max}(\mu_c)$. This is also the EoS exhibiting a phase transition with the largest possible latent heat

$$Q = \mu_c (n_{\max}(\mu_c) - n_{\min}(\mu_c)) = -\mu_L n_L + \mu_H n_H + 2p_L - 2p_H. \quad (10)$$

We further note that there is one EoS that has a constant $c_s^2 = 1$ throughout the whole region, connecting the $n_{\max}(\mu_L)$ and $n_{\min}(\mu_H)$. We denote this special EoS as

$$n_c(\mu) = n_{\max}(\mu_L) \mu / \mu_L = n_{\min}(\mu_H) \mu / \mu_H. \quad (11)$$

Any point along this line maximises the area to the left of the point ($\mu < \mu_0$) and minimizes to the right of the point ($\mu > \mu_0$), so that this line corresponds to the maximal pressure at fixed μ .

III. MAPPING TO THE $\epsilon - p$ PLANE

For every allowed point on the $\mu - n$ -plane, we can find minimal and maximal pressures, $p_{\min/\max}(\mu_0, n_0)$, that can be obtained at that point $\{\mu_0, n_0\}$. Note that this is different from the minimal and maximal pressures ($\Delta p_{\min/\max}$) obtainable at μ_H by an EoS passing through $\{\mu_0, n_0\}$ as discussed in the previous section.

The minimal pressure is given by the EoS that follows the maximally stiff causal line terminating at the point $\{\mu_0, n_{\min}(\mu_0)\}$, i.e., $n(\mu) = \frac{\mu}{\mu_0} n_{\min}(\mu_0)$, and has a phase transition from n_{\min} to n_0 at μ_0 . This construction leads to a lower bound of the pressure as function of μ and n

$$p_{\min}(\mu_0, n_0) = p_L + \frac{\mu_0^2 - \mu_L^2}{2\mu_0} n_{\min}(\mu_0) \quad (12)$$

In order to find the maximal pressure for a given point, the $\mu - n$ plane needs to be divided in two different regions. For $n < n_c(\mu)$ (see eq. (11)), the maximal pressure is obtained by following the maximally stiff causal line terminating at the point itself $n(\mu) = n_0\mu/\mu_0$

$$p_{\max}(\mu_0, n_0) = p_L + \frac{\mu_0^2 - \mu_L^2}{2\mu_0} n_0, \quad n < n_c(\mu). \quad (13)$$

For $n > n_c(\mu)$, the above construction would lead to a pressure that is inconsistent with the integral constraint. Instead, a bound can be obtained by noting that the EoS that maximizes the pressure at $\{\mu_0, n_0\}$ is an EoS that minimizes the pressure difference between μ_0 and μ_H . Thus the maximum pressure in that point is given by the difference between Δp and the pressure for maximally stiff EoS following causal line starting at $\{\mu_0, n_0\}$

$$p_{\max}(\mu_0, n_0) = p_H - \frac{\mu_H^2 - \mu_0^2}{2\mu_0} n_0, \quad n > n_c(\mu). \quad (14)$$

The simultaneous bounds for μ , n and p are visualized in fig. 3. These constraints can be easily translated into bounds on the $\epsilon - p$ -plane using the Euler equation $\epsilon = -p + \mu n$ for a fixed density n . To obtain the envelope of the allowed values of $p(\epsilon)$ irrespective of n (green lines in fig. 1 and fig. 4) we consider lines of constant enthalpy $h = \mu n = \epsilon + p$. Finding the maximum and minimum pressure along these lines maps the bounds from $\mu - n$ to $\epsilon - p$ -plane; for details, see Appendix A.

Figure 1 shows the allowed range of ϵ and p values with and without imposing the high-density constraint for fixed densities of $n = 2, 3, 5$, and $10n_s$ using the $X = 2$ values for pQCD and the “stiff” values for CET. At the lowest density of $n = 2n_s$ the high-density input does not offer additional constraint. However, strikingly, already at $n = 3n_s$ the largest pressures allowed by causality alone are cut off by the integral constraint. At this density only 68% of the $\epsilon - p$ values that would be allowed without the high-density constraint remain (given by the ratio of the blue and combined blue and red areas in fig. 1 when plotted in linear scale, also see fig. A1). At $n = 5n_s$ only 25% of the allowed region remains after imposing the integral constraint. At $n = 10n_s$, the allowed range of values is significantly reduced, now also featuring a cut of the lowest pressures leaving around 6.5% of the total area.

We have checked the stability of these results against variation of different pQCD and CET limits in table I. While varying the CET parameters has a very small effect on the excluded areas (of the order of line width in fig. 1), varying the pQCD renormalization parameter increases the area in $\epsilon - p$ -plane. The union of allowed areas in range $X = [1, 4]$ excludes [13%, 64%, 92.8%] of the otherwise allowed area (without pQCD) for $n = [3, 5, 10] n_s$. For comparison the same numbers for fixed $X = 2$ are [32%, 75%, 93.5%], see fig. A1 in the Appendix. The lowest density at which p and ϵ are limited by the high-density input is $n_{\min}(\mu_L) = [2.2, 2.5] n_s$ for $X = [1, 4]$.

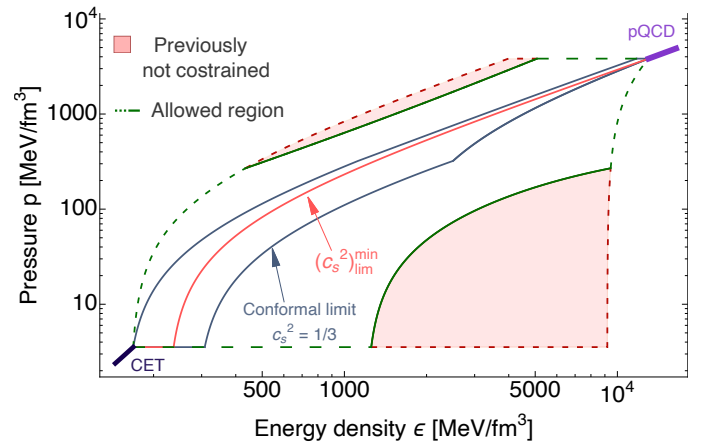


FIG. 4. Constraints to $p(\epsilon)$ for different limiting values of the sound speed. The green envelope corresponds to $c_s^2 = 1$ while the blue envelope corresponds to the conformal limit $c_s^2 = 1/3$. At the specific value of the sound speed $(c_s^2)_{\lim}$ the allowed region degenerates in to a single line. The red areas are not excluded if trivially interpolating the reduced form of the EoS $p(\epsilon)$.

The lowest density where the pressure is limited from below is $n_{\max}(\mu_L) = [4.8, 9.0] n_s$ for the same values of X .

IV. SPEED-OF-SOUND CONSTRAINTS

The EoSs that render the boundaries of the allowed regions in fig. 1 and fig. 2 are composed of the most extreme ones allowed by the above conditions. They contain maximal allowed phase transitions and extended density ranges where the speed of sound coincides with the speed of light. While it is clear that these most extreme EoSs are unlikely to be the physical one, they cannot be excluded with the same level of robustness as those which break the above criteria.

A possible way to quantify how extreme the EoSs are is by imposing a maximal speed of sound $c_s^2 < c_{s,\lim}^2 < 1$ that is reached at any density within the interpolation region [27]. In Appendix B we give the generalizations for $n_{\min/\max}$, $p_{\min/\max}$, and μ_c for arbitrary limiting $c_{s,\lim}^2$. The analysis is similar to that of the above with the modification of maximally stiff causal lines to lines of constant speed of sound $n(\mu) = n_0(\mu/\mu_0)^{1/c_{s,\lim}^2}$.

As the maximum speed of sound is reduced, the allowed range of possible $n(\mu)$ diminishes rapidly leading to tighter bounds on the EoS. This is demonstrated in fig. 4, showing the range of allowed values of $p(\epsilon)$ at different values of $c_{s,\lim}^2$. Interestingly, we note that while the so-called conformal bound — that is, $c_{s,\lim}^2 = 1/3$ — is consistent with the high-density constraint, imposing this condition to the speed of sound gives an extremely strong constraint to the EoS and forces the EoS to have a specific shape at all densities.

Decreasing $c_{s,\text{lim}}^2$ even further, we eventually close the gap between the lower and upper bounds completely, shown in fig. 4 as red line. At this specific value of $c_{s,\text{lim}}^2 = (c_{s,\text{lim}}^2)^{\text{min}}$ the allowed region degenerates into a single line. This is the minimum limiting value for sound speed for which the low- and high- density limits can be connected in a consistent way. Thus $c_s^2 > (c_{s,\text{lim}}^2)^{\text{min}}$ has to be reached by any EoS at some density. For different values of $X = [1, 2, 4]$, we find the minimal limiting values to be just below the conformal limit $[0.32, 0.30, 0.32]$, see Appendix B. It is curious to note that these values are very close to their pQCD values approaching the conformal limit from below even though the pQCD values did not enter the calculation of $(c_{s,\text{lim}}^2)^{\text{min}}$.

V. DISCUSSIONS

Our results demonstrate the non-trivial and robust constraints on the EoS at NS densities arising from pQCD calculations. These constraints are obtained only when interpolating the full EoS $p(\mu)$ instead of its reduced form $p(\epsilon)$.

The results highlight the complementarity of the high- and low-density calculations. This is further demonstrated in fig. 5 depicting the expected effect of future calculations on the allowed region of $\epsilon - p$ -values at $5n_s$ and $10n_s$. We anticipate future results by extrapolating either CET ("stiff") up to $n = 2n_s$ using values tabulated in [62] and/or extrapolating the pQCD results ($X = 2$) of [55] down to $n = 20n_s$ (corresponding to $\mu = 2.1$ GeV). Improvements of this magnitude have been suggested, e.g., in [63, 64]. We see that both the low- and the high-density calculations have a potential to significantly constrain the EoS in the future and that the greatest benefit is obtained by combining the both approaches. Lastly, we note that merely a 7% reduction of the pQCD pressure for $X = 1$ (or using $X = 0.95$) would necessitate the violation of the conformal bound. This implies that an improved pQCD calculations could be used in the future to cleanly rule out all EoSs that remain subconformal at all densities. These results highlight the importance of pursuing both the low- and high-density calculations in the future.

VI. ACKNOWLEDGMENTS

We thank Eemeli Annala, Tyler Gorda, Tore Kleppe, Kai Hebeler, Achim Schwenk, and Aleksu Vuorinen for useful discussions. We also thank Sanjay Reddy for posing questions on multiple occasions about the role of high-density constraints that in part motivated this paper.

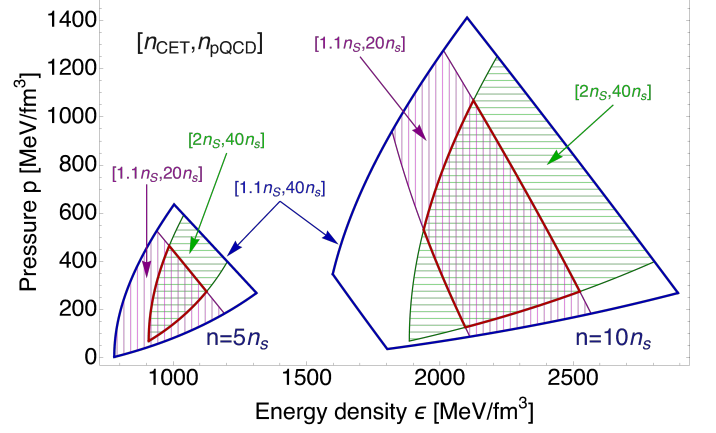


FIG. 5. The expected impact of future calculations on the theoretical constraints to ϵ and p at NS densities obtained by extrapolating the CET and pQCD calculations to intermediate densities. Numbers in square bracket show the end point of extrapolation of the CET and pQCD calculations. Blue areas denoted as $[1.1n_s, 40n_s]$ correspond to blue area in fig. 1. Green areas are extrapolation of CET limit up to $2n_s$ [62], while purple regions are extrapolations of pQCD down to $20n_s$ [55]. The combined effect of extrapolating both limits is given by the overlapping region.

Appendix A: Boundaries on the $\epsilon - p$ -plane

Utilizing the Euler equation $\epsilon = -p + \mu n$, one can map bounds from $\mu - n$ -plane to the corresponding limits on the $\epsilon - p$ -plane. In order to find the extremal allowed values of $p(\epsilon)$, consider lines of fixed enthalpy $h = \epsilon + p = \mu n$. These lines correspond on one hand to diagonal lines $p(\epsilon) = -\epsilon + h$ on the $\epsilon - p$ -plane, and on the other hand to hyperbolas $n(\mu) = h/\mu$ on the $\mu - n$ -plane. Therefore, minimising or maximizing the pressure for a constant h on the $\mu - n$ -plane gives the minimal and maximal pressure on the corresponding isenthalpic line on the $\epsilon - p$ -plane.

Substituting $n = h/\mu$ in eq. (12) we readily observe that the smallest minimal pressure along isenthalpic line, $p_{\text{min}}(\mu, h/\mu)$, is obtained at smallest value μ allowed by the constraints, that is, at the crossing of the isenthalpic line and $n_{\text{max}}(\mu)$.

Similarly, substituting $n = h/\mu$ in eq. (13) and eq. (14) we observe that the maximal pressure $p_{\text{max}}(\mu, h/\mu)$ obtains its largest value for the largest value μ allowed, at the crossing of the isenthalpic line and $n_{\text{min}}(\mu)$.

Therefore the allowed range of values in the $\epsilon - p$ -plane is bounded from below by the line $\{\epsilon_{\text{max}}(\mu), p_{\text{min}}(\mu, n_{\text{max}}(\mu))\}$ with $\mu_L < \mu < \mu_H$, where

$$\begin{aligned} \epsilon_{\text{max}}(\mu) &= -p_{\text{min}}(\mu, n_{\text{max}}(\mu)) + \mu n_{\text{max}}(\mu) \\ &= \begin{cases} \frac{(\mu^2 + \mu_H^2)(\mu^2 n_L + \mu_L(2p_L - \mu_L n_L)) - 4\mu^2 \mu_L p_H}{2\mu_L(\mu - \mu_H)(\mu + \mu_H)}, & \mu < \mu_c \\ \frac{1}{2}((\mu^2 n_H)/\mu_H + \mu_H n_H - 2p_H), & \mu > \mu_c. \end{cases} \end{aligned} \quad (\text{A1})$$

This corresponds to the lower bound in fig. 1 and fig. 4. In fig. 3, the line $\{\mu, n_{\text{max}}(\mu), p_{\text{min}}(\mu, n_{\text{max}}(\mu))\}$ corresponds

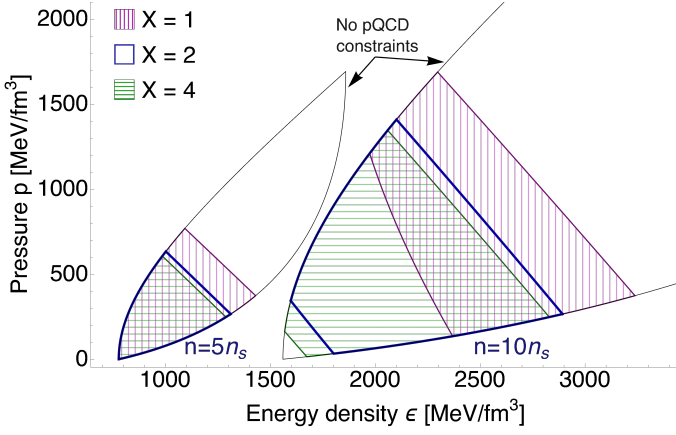


FIG. A1. The impact of the pQCD renormalization parameter variation on the theoretical constraints to ϵ and p at NS densities. Blue area denoted as $X = 2$ corresponds to blue area in fig. 1. Purple and green areas correspond to allowed area for renormalization parameter $X = 1$ and $X = 4$, respectively. Thin black line corresponds to allowed area without high-density input.

to the dashed green line marked n_{\max} .

Similarly the allowed $\epsilon - p$ values are bounded by above by $\{\epsilon_{\min}(\mu), p_{\max}(\mu, n_{\min}(\mu_B))\}$, with

$$\epsilon_{\min}(\mu) = -p_{\max}(\mu, n_{\min}(\mu)) + \mu n_{\min}(\mu) \quad (\text{A2})$$

$$= \begin{cases} \frac{1}{2}((\mu^2 n_L)/\mu_L + \mu_L n_L - 2p_L) & \mu < \mu_c \\ \frac{\mu_L^4}{\mu_L^2} \frac{n_H}{\mu_H} + (\frac{\mu}{\mu_L})^2 (\mu_L^2 \frac{n_H}{\mu_H} - \mu_H n_H + 4p_L - 2p_H) + 2p_H - \mu_H n_H & \mu > \mu_c \end{cases}$$

This corresponds to the upper bound of pressure in fig. 1 and fig. 4. In fig. 3, the line $\{\mu, n_{\min}(\mu), p_{\max}(\mu, n_{\min}(\mu))\}$ corresponds to the dashed green line marked n_{\min} .

Additionally, in fig. A1 we present the impact of the pQCD renormalization parameter variation on the allowed area for the fixed number density $5n_s$ and $10n_s$. It can be readily seen from the figure that for $5n_s$ pQCD input excludes 65% (for $X = 1$) of the otherwise allowed area, and for $X = 2$ only 25% of the $\epsilon - p$ values is allowed. The expressions for the areas without pQCD constraints are easily obtained by sending $\mu_c \rightarrow \infty$ and $n_c \rightarrow \infty$ and so taking the expressions corresponding to $\mu < \mu_c$ and $n < n_c$.

Appendix B: Boundaries with arbitrary $c_{s,\text{lim}}^2$

In this appendix we give generalizations of the bounds discussed in the main text for limiting speed of sound $c_{s,\text{lim}}^2 = 1$ to arbitrary $c_{s,\text{lim}}^2$.

The line with the constant speed of sound is given by

$$n(\mu) = n_0(\mu/\mu_0)^{1/c_s^2}. \quad (\text{B1})$$

The assumption that no EoS is allowed to be stiffer than this with the additionally imposed integral constraints

leads to the minimal and maximal densities at fixed μ

$$n_{\min} = \begin{cases} n_L \left(\frac{\mu}{\mu_L} \right)^{1/c_s^2}, & \mu < \mu_c \\ \frac{\left(\frac{\mu}{\mu_L} \right)^{1/c_s^2} \left(c_s^2 \left(\mu n_H \left(\frac{\mu}{\mu_H} \right)^{1/c_s^2} - \mu_H n_H + \Delta p \right) + \Delta p \right)}{c_s^2 \left(\mu \left(\frac{\mu}{\mu_L} \right)^{1/c_s^2} - \mu_L \right)}, & \mu > \mu_c \end{cases} \quad (\text{B2})$$

and

$$n_{\max} = \begin{cases} \frac{\left(\frac{\mu}{\mu_H} \right)^{1/c_s^2} \left(c_s^2 \left(\mu n_L \left(\frac{\mu}{\mu_L} \right)^{1/c_s^2} - \mu_L n_L - \Delta p \right) - \Delta p \right)}{c_s^2 \left(\mu \left(\frac{\mu}{\mu_H} \right)^{1/c_s^2} - \mu_H \right)}, & \mu < \mu_c \\ n_H \left(\frac{\mu}{\mu_H} \right)^{1/c_s^2}, & \mu > \mu_c \end{cases} \quad (\text{B3})$$

where

$$\mu_c = \left(\frac{\mu_H^{1/c_s^2} (c_s^2 (\mu_L n_L - \mu_H n_H + \Delta p) + \Delta p)}{c_s^2 \left(n_L \left(\frac{\mu_H}{\mu_L} \right)^{1/c_s^2} - n_H \right)} \right)^{\frac{c_s^2}{c_s^2 + 1}}. \quad (\text{B4})$$

For any given μ the largest allowed latent heat associated to a phase transition is given by

$$Q(\mu) = \mu(n_{\max}(\mu) - n_{\min}(\mu)) \quad (\text{B5})$$

$$= \frac{\mu \left(\frac{\mu}{\mu_L \mu_H} \right)^{1/c_s^2} \left(c_s^2 n_L \mu_H^{\frac{1}{c_s^2} + 1} - \mu_L^{1/c_s^2} (c_s^2 (\mu_L n_L + \Delta p) + \Delta p) \right)}{c_s^2 \left(\mu \left(\frac{\mu}{\mu_H} \right)^{1/c_s^2} - \mu_H \right)}$$

for $\mu < \mu_c$. For $\mu > \mu_c$ the expression is obtained by changing $H \leftrightarrow L$ in the above expression and multiplying the whole expression by -1. The phase transition with largest allowed latent heat takes place at $\mu = \mu_c$ and has the latent heat

$$Q = \epsilon_H - \epsilon_L - \frac{p_H - p_L}{c_s^2}. \quad (\text{B6})$$

The line with largest pressure at fixed μ is given by

$$n_c(\mu) = n_{\max}(\mu_L) \left(\frac{\mu}{\mu_L} \right)^{1/c_s^2}. \quad (\text{B7})$$

The minimal and maximal pressures at given point $\{\mu_0, n_0\}$ generalize simply to

$$p_{\min}(\mu_0, n_0) = p_L + \frac{c_s^2}{1 + c_s^2} \left[\mu_0 - \mu_L \left(\frac{\mu_L}{\mu_0} \right)^{1/c_s^2} \right] n_{\min}(\mu_0) \quad (\text{B8})$$

and for $n_0 < n_c(\mu_0)$

$$p_{\max}(\mu_0, n_0) = p_L + \frac{c_s^2}{1 + c_s^2} \left[\mu_0 - \mu_L \left(\frac{\mu_L}{\mu_0} \right)^{1/c_s^2} \right] n_0 \quad (\text{B9})$$

and for $n_0 > n_c(\mu_0)$

$$p_{\max}(\mu_0, n_0) = p_H + \frac{c_s^2}{1 + c_s^2} \left[\mu_0 - \mu_H \left(\frac{\mu_H}{\mu_0} \right)^{1/c_s^2} \right] n_0. \quad (\text{B10})$$

Reducing the $c_{s,\text{lim}}^2$, the allowed values of $n(\mu)$ eventually degenerate into a line. This line is either a line of constant speed of sound starting from $\{\mu_L, n_L\}$ with a phase transition at μ_H , or a line of constant speed of sound terminating to $\{\mu_H, n_H\}$ with a phase transition at μ_L . Which of these cases is realised depends on the input parameter values, the criteria for it is given by

$$\frac{p_H - p_L}{\epsilon_h - \epsilon_l} = \frac{\log(\mu_H/\mu_L)}{\log(n_H/n_L)}. \quad (\text{B11})$$

If the left hand side of the eq. (B11) is bigger than

right hand side than the value for $(c_s^2)_{\text{lim}}^{\min}$ is given by the solution of the equation

$$\int_{\mu_L}^{\mu_H} d\mu n_H \left(\frac{\mu}{\mu_H} \right)^{1/(c_s^2)_{\text{lim}}^{\min}} = \Delta p. \quad (\text{B12})$$

Otherwise the equation reads

$$\int_{\mu_L}^{\mu_H} d\mu n_L \left(\frac{\mu}{\mu_L} \right)^{1/(c_s^2)_{\text{lim}}^{\min}} = \Delta p. \quad (\text{B13})$$

In general, these equations need to be solved numerically. The another way of computing $(c_s^2)_{\text{lim}}^{\min}$ would be finding which of these cases happen first. Instead of using criteria eq. (B11) one can solve both eqs. (B12), (B13) and take maximum of the solutions in order to find $(c_s^2)_{\text{lim}}^{\min}$.

-
- [1] M. C. Miller *et al.*, The radius of PSR J0740+6620 from NICER and XMM-Newton data, *Astrophys. J. Lett.* **918**, L28 (2021), [arXiv:2105.06979 \[astro-ph.HE\]](#).
 - [2] T. E. Riley *et al.*, A NICER view of the massive pulsar PSR J0740+6620 informed by radio timing and XMM-Newton spectroscopy, *Astrophys. J. Lett.* **918**, L27 (2021), [arXiv:2105.06980 \[astro-ph.HE\]](#).
 - [3] P. B. Demorest, T. Pennucci, S. M. Ransom, M. S. E. Roberts, and J. H. T. Hessels, A two-solar-mass neutron star measured using Shapiro delay, *Nature* **467**, 1081 (2010), [arXiv:1010.5788 \[astro-ph.HE\]](#).
 - [4] J. Antoniadis *et al.*, A massive pulsar in a compact relativistic binary, *Science* **340**, 1233232 (2013), [arXiv:1304.6875 \[astro-ph.HE\]](#).
 - [5] E. Fonseca *et al.*, Refined Mass and Geometric Measurements of the High-mass PSR J0740+6620, *Astrophys. J. Lett.* **915**, L12 (2021), [arXiv:2104.00880 \[astro-ph.HE\]](#).
 - [6] B. P. Abbott *et al.*, GW170817: Observation of gravitational waves from a binary neutron star inspiral, *Phys. Rev. Lett.* **119**, 161101 (2017), [arXiv:1710.05832 \[gr-qc\]](#).
 - [7] B. P. Abbott *et al.*, Multi-messenger observations of a binary neutron star merger, *Astrophys. J. Lett.* **848**, L12 (2017), [arXiv:1710.05833 \[astro-ph.HE\]](#).
 - [8] R. C. Tolman, Static solutions of Einstein's field equations for spheres of fluid, *Phys. Rev.* **55**, 364 (1939).
 - [9] J. R. Oppenheimer and G. M. Volkoff, On massive neutron cores, *Phys. Rev.* **55**, 374 (1939).
 - [10] E. Annala, T. Gorda, A. Kurkela, and A. Vuorinen, Gravitational-wave constraints on the neutron-star-matter equation of state, *Phys. Rev. Lett.* **120**, 172703 (2018), [arXiv:1711.02644 \[astro-ph.HE\]](#).
 - [11] B. Margalit and B. D. Metzger, Constraining the maximum mass of neutron stars from multi-messenger observations of GW170817, *Astrophys. J. Lett.* **850**, L19 (2017), [arXiv:1710.05938 \[astro-ph.HE\]](#).
 - [12] L. Rezzolla, E. R. Most, and L. R. Weih, Using gravitational-wave observations and quasi-universal relations to constrain the maximum mass of neutron stars, *Astrophys. J. Lett.* **852**, L25 (2018), [arXiv:1711.00314 \[astro-ph.HE\]](#).
 - [13] M. Ruiz, S. L. Shapiro, and A. Tsokaros, GW170817, general relativistic magnetohydrodynamic simulations, and the neutron star maximum mass, *Phys. Rev. D* **97**, 021501(R) (2018), [arXiv:1711.00473 \[astro-ph.HE\]](#).
 - [14] A. Bauswein, O. Just, H.-T. Janka, and N. Stergioulas, Neutron-star radius constraints from GW170817 and future detections, *Astrophys. J. Lett.* **850**, L34 (2017), [arXiv:1710.06843 \[astro-ph.HE\]](#).
 - [15] D. Radice, A. Perego, F. Zappa, and S. Bernuzzi, GW170817: Joint constraint on the neutron star equation of state from multimessenger observations, *Astrophys. J. Lett.* **852**, L29 (2018), [arXiv:1711.03647 \[astro-ph.HE\]](#).
 - [16] E. R. Most, L. R. Weih, L. Rezzolla, and J. Schaffner-Bielich, New constraints on radii and tidal deformabilities of neutron stars from GW170817, *Phys. Rev. Lett.* **120**, 261103 (2018), [arXiv:1803.00549 \[gr-qc\]](#).
 - [17] T. Dietrich, M. W. Coughlin, P. T. H. Pang, M. Bulla, J. Heinzel, L. Issa, I. Tews, and S. Antier, Multimessenger constraints on the neutron-star equation of state and the Hubble constant, *Science* **370**, 1450 (2020), [arXiv:2002.11355 \[astro-ph.HE\]](#).
 - [18] C. D. Capano, I. Tews, S. M. Brown, B. Margalit, S. De, S. Kumar, D. A. Brown, B. Krishnan, and S. Reddy, Stringent constraints on neutron-star radii from multimessenger observations and nuclear theory, *Nat. Astron.* **4**, 625 (2020), [arXiv:1908.10352 \[astro-ph.HE\]](#).
 - [19] P. Landry and R. Essick, Nonparametric inference of the neutron star equation of state from gravitational wave observations, *Phys. Rev. D* **99**, 084049 (2019), [arXiv:1811.12529 \[gr-qc\]](#).
 - [20] C. A. Raithel, F. Özel, and D. Psaltis, Tidal deformability from GW170817 as a direct probe of the neutron star radius, *Astrophys. J. Lett.* **857**, L23 (2018), [arXiv:1803.07687 \[astro-ph.HE\]](#).
 - [21] C. A. Raithel and F. Özel, Measurement of the nuclear symmetry energy parameters from gravitational-wave events, *Astrophys. J.* **885**, 121 (2019), [arXiv:1908.00018 \[astro-ph.HE\]](#).
 - [22] G. Raaijmakers *et al.*, Constraining the dense matter equation of state with joint analysis of NICER and

- LIGO/Virgo measurements, *Astrophys. J. Lett.* **893**, L21 (2020), [arXiv:1912.11031 \[astro-ph.HE\]](#).
- [23] R. Essick, P. Landry, and D. E. Holz, Nonparametric inference of neutron star composition, equation of state, and maximum mass with GW170817, *Phys. Rev. D* **101**, 063007 (2020), [arXiv:1910.09740 \[astro-ph.HE\]](#).
- [24] M. Al-Mamun, A. W. Steiner, J. Nättilä, J. Lange, R. O’Shaughnessy, I. Tews, S. Gandolfi, C. Heinke, and S. Han, Combining electromagnetic and gravitational-wave constraints on neutron-star masses and radii, *Phys. Rev. Lett.* **126**, 061101 (2021), [arXiv:2008.12817 \[astro-ph.HE\]](#).
- [25] R. Essick, I. Tews, P. Landry, and A. Schwenk, Astrophysical constraints on the symmetry energy and the neutron skin of ^{208}Pb with minimal modeling assumptions, [arXiv:2102.10074 \[nucl-th\]](#) (2021).
- [26] V. Paschalidis, K. Yagi, D. Alvarez-Castillo, D. B. Blaschke, and A. Sedrakian, Implications from GW170817 and I-Love-Q relations for relativistic hybrid stars, *Phys. Rev. D* **97**, 084038 (2018), [arXiv:1712.00451 \[astro-ph.HE\]](#).
- [27] E. Annala, T. Gorda, A. Kurkela, J. Nättilä, and A. Vuorinen, Evidence for quark-matter cores in massive neutron stars, *Nat. Phys.* **16**, 907 (2020), [arXiv:1903.09121 \[astro-ph.HE\]](#).
- [28] M. Ferreira, R. Câmara Pereira, and C. Providência, Quark matter in light neutron stars, *Phys. Rev. D* **102**, 083030 (2020), [arXiv:2008.12563 \[nucl-th\]](#).
- [29] T. Minamikawa, T. Kojo, and M. Harada, Quark-hadron crossover equations of state for neutron stars: Constraining the chiral invariant mass in a parity doublet model, *Phys. Rev. C* **103**, 045205 (2021), [arXiv:2011.13684 \[nucl-th\]](#).
- [30] S. Blacker, N.-U. F. Bastian, A. Bauswein, D. B. Blaschke, T. Fischer, M. Oertel, T. Soutanis, and S. Typel, Constraining the onset density of the hadron-quark phase transition with gravitational-wave observations, *Phys. Rev. D* **102**, 123023 (2020), [arXiv:2006.03789 \[astro-ph.HE\]](#).
- [31] G. Baym, T. Hatsuda, T. Kojo, P. D. Powell, Y. Song, and T. Takatsuka, From hadrons to quarks in neutron stars: a review, *Rept. Prog. Phys.* **81**, 056902 (2018), [arXiv:1707.04966 \[astro-ph.HE\]](#).
- [32] S. Gandolfi, J. Lippuner, A. W. Steiner, I. Tews, X. Du, and M. Al-Mamun, From the microscopic to the macroscopic world: from nucleons to neutron stars, *J. Phys. G* **46**, 103001 (2019), [arXiv:1903.06730 \[nucl-th\]](#).
- [33] C. A. Raithel, Constraints on the neutron star equation of state from GW170817, *Eur. Phys. J. A* **55**, 80 (2019), [arXiv:1904.10002 \[astro-ph.HE\]](#).
- [34] C. J. Horowitz, Neutron rich matter in the laboratory and in the heavens after GW170817, *Annals Phys.* **411**, 167992 (2019), [arXiv:1911.00411 \[astro-ph.HE\]](#).
- [35] L. Baiotti, Gravitational waves from neutron star mergers and their relation to the nuclear equation of state, *Prog. Part. Nucl. Phys.* **109**, 103714 (2019), [arXiv:1907.08534 \[astro-ph.HE\]](#).
- [36] K. Chatziioannou, Neutron star tidal deformability and equation-of-state constraints, *Gen. Rel. Grav.* **52**, 109 (2020), [arXiv:2006.03168 \[gr-qc\]](#).
- [37] D. Radice, S. Bernuzzi, and A. Perego, The dynamics of binary neutron star mergers and GW170817, *Ann. Rev. Nucl. Part. Sci.* **70**, 95 (2020), [arXiv:2002.03863 \[astro-ph.HE\]](#).
- [38] I. Goldman and S. Nussinov, Weakly Interacting Massive Particles and Neutron Stars, *Phys. Rev. D* **40**, 3221 (1989).
- [39] G. F. Giudice, M. McCullough, and A. Urbano, Hunting for Dark Particles with Gravitational Waves, *JCAP* **10**, 001, [arXiv:1605.01209 \[hep-ph\]](#).
- [40] P. Ciarcelluti and F. Sandin, Have neutron stars a dark matter core?, *Phys. Lett. B* **695**, 19 (2011), [arXiv:1005.0857 \[astro-ph.HE\]](#).
- [41] A. Li, F. Huang, and R.-X. Xu, Too massive neutron stars: The role of dark matter?, *Astropart. Phys.* **37**, 70 (2012), [arXiv:1208.3722 \[astro-ph.SR\]](#).
- [42] Q.-F. Xiang, W.-Z. Jiang, D.-R. Zhang, and R.-Y. Yang, Effects of fermionic dark matter on properties of neutron stars, *Phys. Rev. C* **89**, 025803 (2014), [arXiv:1305.7354 \[astro-ph.SR\]](#).
- [43] L. Tolos and J. Schaffner-Bielich, Dark Compact Planets, *Phys. Rev. D* **92**, 123002 (2015), [Erratum: *Phys. Rev. D* **103**, 109901 (2021)], [arXiv:1507.08197 \[astro-ph.HE\]](#).
- [44] J. Ellis, G. Hütsi, K. Kannike, L. Marzola, M. Raidal, and V. Vaskonen, Dark Matter Effects On Neutron Star Properties, *Phys. Rev. D* **97**, 123007 (2018), [arXiv:1804.01418 \[astro-ph.CO\]](#).
- [45] A. Del Popolo, M. Le Delliou, and M. Deliyergiyev, Neutron Stars and Dark Matter, *Universe* **6**, 222 (2020).
- [46] J. C. Jiménez and E. S. Fraga, Radial oscillations of quark stars admixed with dark matter, (2021), [arXiv:2111.00091 \[hep-ph\]](#).
- [47] T. Damour and G. Esposito-Farese, Nonperturbative strong field effects in tensor - scalar theories of gravitation, *Phys. Rev. Lett.* **70**, 2220 (1993).
- [48] X.-T. He, F. J. Fattoyev, B.-A. Li, and W. G. Newton, Impact of the equation-of-state-gravity degeneracy on constraining the nuclear symmetry energy from astrophysical observables, *Phys. Rev. C* **91**, 015810 (2015), [arXiv:1408.0857 \[nucl-th\]](#).
- [49] M. Aparicio Resco, A. de la Cruz-Dombriz, F. J. Llanes Estrada, and V. Zapatero Castrillo, On neutron stars in $f(R)$ theories: Small radii, large masses and large energy emitted in a merger, *Phys. Dark Univ.* **13**, 147 (2016), [arXiv:1602.03880 \[gr-qc\]](#).
- [50] D. D. Doneva, S. S. Yazadjiev, N. Stergioulas, and K. D. Kokkotas, Differentially rotating neutron stars in scalar-tensor theories of gravity, *Phys. Rev. D* **98**, 104039 (2018), [arXiv:1807.05449 \[gr-qc\]](#).
- [51] E. Lope Oter, A. Windisch, F. J. Llanes-Estrada, and M. Alford, nEoS: Neutron Star Equation of State from hadron physics alone, *J. Phys. G* **46**, 084001 (2019), [arXiv:1901.05271 \[gr-qc\]](#).
- [52] I. Tews, T. Krüger, K. Hebeler, and A. Schwenk, Neutron matter at next-to-next-to-next-to-leading order in chiral effective field theory, *Phys. Rev. Lett.* **110**, 032504 (2013), [arXiv:1206.0025 \[nucl-th\]](#).
- [53] C. Drischler, K. Hebeler, and A. Schwenk, Chiral interactions up to next-to-next-to-next-to-leading order and nuclear saturation, *Phys. Rev. Lett.* **122**, 042501 (2019), [arXiv:1710.08220 \[nucl-th\]](#).
- [54] T. Gorda, A. Kurkela, P. Romatschke, M. Säppi, and A. Vuorinen, Next-to-next-to-next-to-leading order pressure of cold quark matter: Leading logarithm, *Phys. Rev. Lett.* **121**, 202701 (2018), [arXiv:1807.04120 \[hep-ph\]](#).
- [55] T. Gorda, A. Kurkela, R. Paatelainen, S. Säppi, and A. Vuorinen, Soft Interactions in Cold Quark Matter, *Phys. Rev. Lett.* **127**, 162003 (2021), [arXiv:2103.05658](#)

- [56] A. Kurkela, E. S. Fraga, J. Schaffner-Bielich, and A. Vuorinen, Constraining neutron star matter with Quantum Chromodynamics, *Astrophys. J.* **789**, 127 (2014), [arXiv:1402.6618 \[astro-ph.HE\]](#).
- [57] E. Annala, T. Gorda, E. Katerini, A. Kurkela, J. Nättilä, V. Paschalidis, and A. Vuorinen, Multimessenger constraints for ultra-dense matter, (2021), [arXiv:2105.05132 \[astro-ph.HE\]](#).
- [58] C. E. Rhoades, Jr. and R. Ruffini, Maximum mass of a neutron star, *Phys. Rev. Lett.* **32**, 324 (1974).
- [59] S. Koranda, N. Stergioulas, and J. L. Friedman, Upper limit set by causality on the rotation and mass of uniformly rotating relativistic stars, *Astrophys. J.* **488**, 799 (1997), [arXiv:astro-ph/9608179](#).
- [60] I. Tews, J. Margueron, and S. Reddy, Confronting gravitational-wave observations with modern nuclear physics constraints, *Eur. Phys. J. A* **55**, 97 (2019), [arXiv:1901.09874 \[nucl-th\]](#).
- [61] E. Lope-Oter and F. J. Llanes-Estrada, Maximum latent heat of neutron star matter independently of General Relativity, (2021), [arXiv:2103.10799 \[nucl-th\]](#).
- [62] K. Hebeler, J. M. Lattimer, C. J. Pethick, and A. Schwenk, Equation of state and neutron star properties constrained by nuclear physics and observation, *Astrophys. J.* **773**, 11 (2013), [arXiv:1303.4662 \[astro-ph.SR\]](#).
- [63] Y. Fujimoto and K. Fukushima, Equation of state of cold and dense QCD matter in resummed perturbation theory, (2020), [arXiv:2011.10891 \[hep-ph\]](#).
- [64] L. Fernandez and J.-L. Kneur, All order resummed leading and next-to-leading soft modes of dense QCD pressure, (2021), [arXiv:2109.02410 \[hep-ph\]](#).